ACCOUNTS
of chemical research

Microparticle Electrodes and Single Particle Microbatteries: Electrochemical and in Situ MicroRaman Spectroscopic Studies

ADRIEL JEBIN JACOB JEBARAJ AND DANIEL A. SCHERSON*

The Ernest B. Yeager Center for Electrochemical Sciences and The Department of Chemistry, Case Western Reserve University, Cleveland, Ohio 44106-7078, United States

RECEIVED ON JULY 16, 2012

CONSPECTUS

Studies of the intrinsic electrochemical, structural, and electronic properties of microparticles of energy storage materials can provide much needed insight into the factors that control various aspects of the performance of technical electrodes for battery applications. This Account summarizes efforts made in our laboratories toward the development and implementation of methods for the in situ electrical, optical, and spectroscopic characterization of microparticles of a variety of such materials, including Ni hydroxide, Zn, carbon, and lithiated Mn and Co oxides. In the case of Ni hydroxide, the much darker appearance of NiOOH compared to the virtually translucent character of virgin $Ni(OH)_2$ allowed for the spatial and temporal evolution of charge flow within spherical microparticles of $Ni(OH)_2$ to be monitored in real time during the first scan toward positive potentials using computer-controlled video imaging. In situ Raman scattering measurements involving single microparticles of Zn harvested from a commercial $Zn|MnO_2$ battery revealed that passive films formed in strongly alkaline solutions by stepping the potential from 1.55 V to either 0.7 or 0.8 V vs SCE displayed a largely enhanced feature at ca. 565 cm^{-1} ascribed to a longitudinal optical phonon mode of ZnO, an effect associated with the presence of interstitial Zn and oxygen deficiencies in the lattice. In addition, significant amounts of crystalline ZnO could be detected only for passive films formed at the same two potentials after the electrodes had been roughened by a single passivation−reduction step. Quantitative correlations were found in the case of $LiMn_2O_4$ and KS-44 graphite between the Raman spectral properties and the state of charge. In the case of KS-44, a chemometrics analysis of the spectroscopic data in the potential region in which the transition between dilute phase 1 and phase 4 of lithiated graphite is known to occur made it possible to determine *independently* the fraction of each of the two phases present as a function of potential without relying on the coulometric information. Also featured in this Account are methods we developed for the assembly and electrochemical characterization of $Zn|MnO_2$ and nickel|metal-hydride Ni|MH alkaline batteries incorporating single microparticles of the active materials. As evidenced from the data collected, the voltage−time profiles for constant current operation for both types of devices were found to be similar to those of commercially available batteries involving the same chemistries. The ability to monitor the state of charge of individual particles based strictly on spectroscopic data is expected to open exciting new prospects for visualizing the flow of charge within electrodes in Li-ion batteries, an area that is being vigorously pursued in our laboratories.

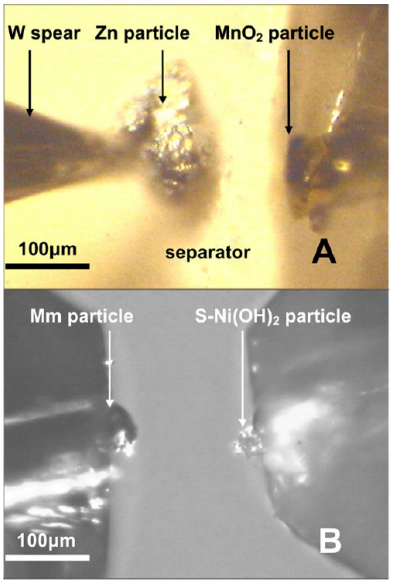

Introduction

Over the last two to three decades, batteries have become among the most ubiquitous devices ever invented. Powering this explosive growth is the increasing popularity of novel and ever more sophisticated hand-held cellular phones, personal computers, and entertainment electronics. Electrodes in portable rechargeable batteries are composed mainly of particles of micrometer dimensions responsible for the interconversion of electrical and chemical energy through changes in the oxidation state of one or

Published on the Web 03/26/2013 www.pubs.acs.org/accounts
10.1021/ar300210q

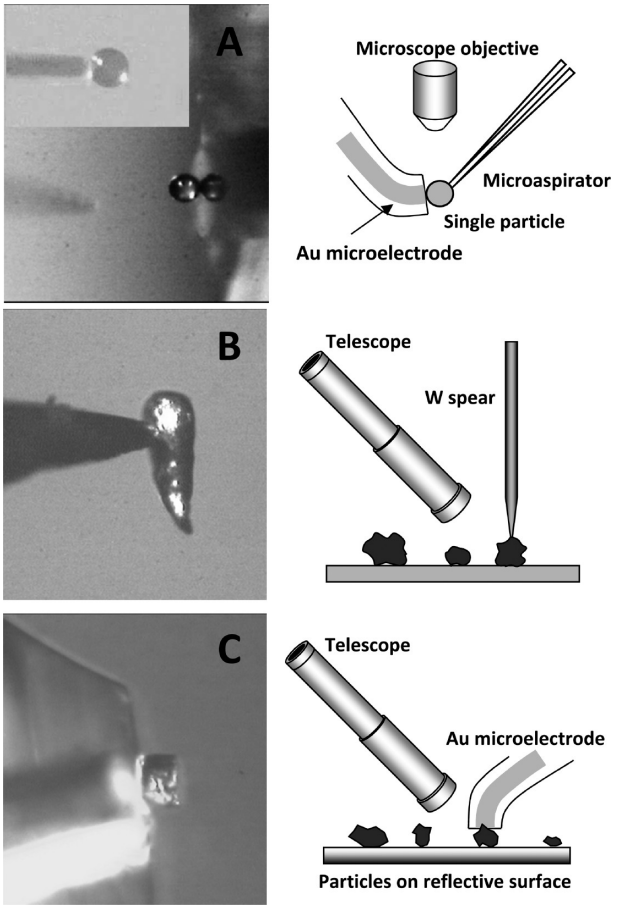

FIGURE 1. Micrographs (left) and schematic diagrams (right) of single microparticles attached to the micropipet (panel A), the W spear (panel B), and embedded in a microelectrode (panel C).

more of its constituent elements.[1] Technical electrodes usually incorporate other components, such as conductivity enhancers, for example, high area carbon, and organic binders, to form a mechanically robust, electrically continuous pastelike material that can be applied to the current collector. Although essential to achieving high performance, the presence of these additives and the resulting complex electrode architectures make it very difficult to extract information regarding the intrinsic properties of the charge storage materials themselves. This Account reviews efforts in our laboratories, aimed at the development and implementation of techniques for monitoring in situ the optical, spectroscopic, and electrical properties of individual charge storage microparticles and single microparticle batteries under conditions that approximate those found in commercial devices, and represent an extension of the work of Prof. I. Uchida at Tohoku University, Japan, who published seminal papers in the area of single microparticle electrochemistry.[2,3] Extensive use was made of Raman microscopy,

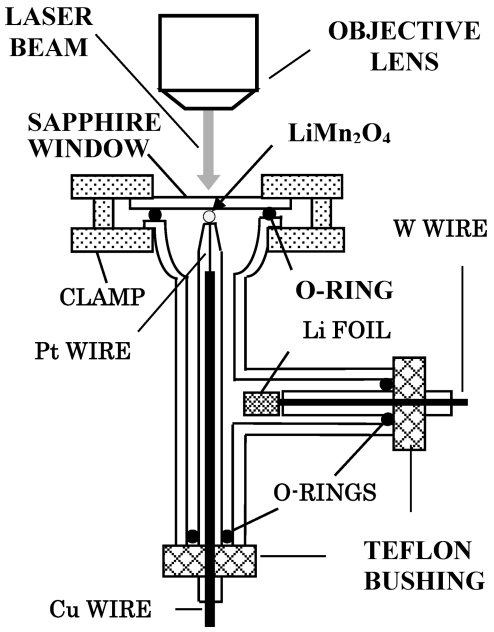

FIGURE 2. Schematic diagram of a spectroelectrochemical cell for acquisition of simultaneous in situ Raman and cyclic voltammetric measurements of single particle microelectrodes.

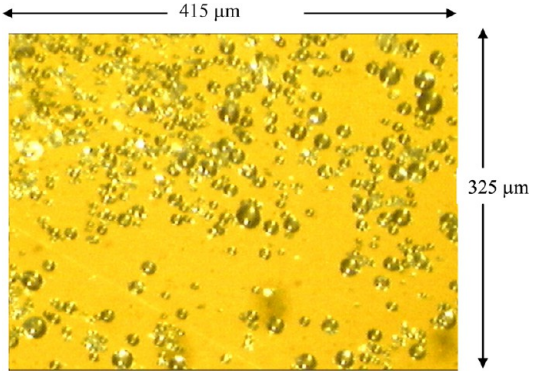

FIGURE 3. Image of a collection of s-$Ni(OH)_2$ particles.

a technique that allows analysis of small sample areas or volumes down to the micrometer scale.[4]

Experimental Considerations

Critical to the characterization of single μ-particle electrodes and the assembly of single particle μ-batteries is the ability of placing μ-particles in contact with an electronic conducting support. A few illustrations of the strategies we have developed to manipulate μ-particles include[5] a glass capillary attached to a syringe (not shown), which allows fragile particles to be captured by suction and then delivered to the substrate surface (panel A, Figure 1), a sharp spear of a hard metal, that can be inserted into a softer malleable material (panel B), and a μ-disk electrode made out of a soft metal, into which hard particles can be embedded by

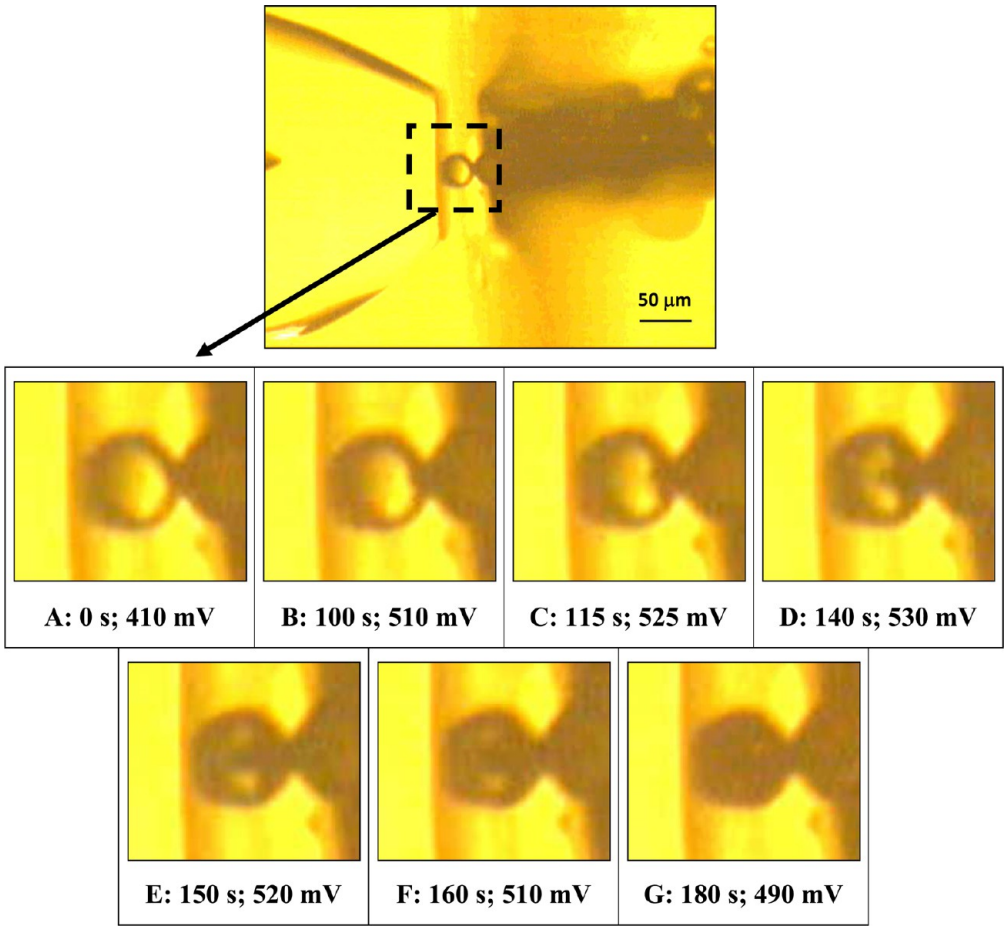

FIGURE 4. Images obtained in sequence at the specified times/potentials during a video session in which the optical properties of the s-$Ni(OH)_2$ particle ca. 34 μm in diameter were monitored during the first voltammetric cycle at 1 mV/s. Video recording was started at 0.410 V vs SCE during the positive going scan.

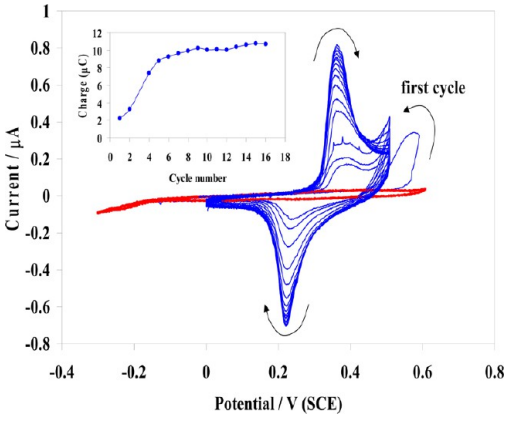

FIGURE 5. Series of consecutive voltammetric cycles for a single s-$Ni(OH)_2$ particle 30 μm in diameter. The rather featureless trace in red was obtained for a Au microelectrode under the same conditions.

applying pressure (panel C). In addition, the substrate should exhibit a low and featureless capacitance within the potential range in which the charge storage material undergoes changes in redox state. Because of the small size of the materials involved, all manipulation and assembly operations must be performed under a microscope (or, at times, a telescope). Most of the Raman spectra were collected with a Raman 2000 system (Chromex, Inc.), using a Verdi laser (532 nm) focused through an Olympus microscope as the excitation source. An all-glass, airtight, spectroelectrochemical cell (see Figure 2)[6] was constructed for studies in nonaqueous electrolytes.

A. Single Microparticle Electrode Studies. 1. Aqueous Systems. a. Spherical $Ni(OH)_2$. Nickel hydroxide is a charge storage cathode material for rechargeable batteries that power the vast majority of hybrid vehicles on the road today. In its pristine form, this material consists of transparent spheres of diameters in the micrometer range (see Figure 3), which can be easily captured in air using a μ-pipet (see inset, panel A, Figure 1). A glass truncated cone is used to apply pressure on the particle|μ-disk assembly to keep the μ-particle in place (see Figure 4, upper panel).[7] Prior to the experiments, the tool|μ-particle|μ-electrode assembly was immersed in a Petri dish

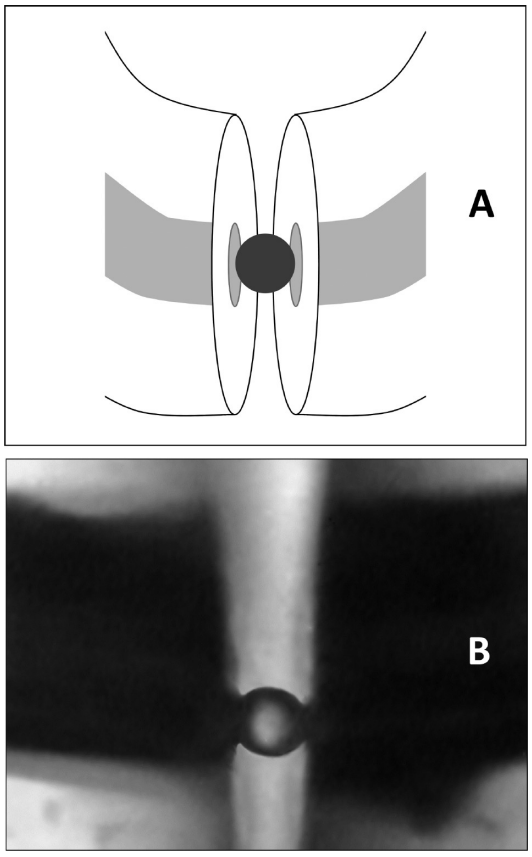

FIGURE 6. Schematic drawing (panel A) and microphotograph (panel B) of the assembly developed for in situ resistance measurements of single particle microelectrodes as a function of their state of charge.

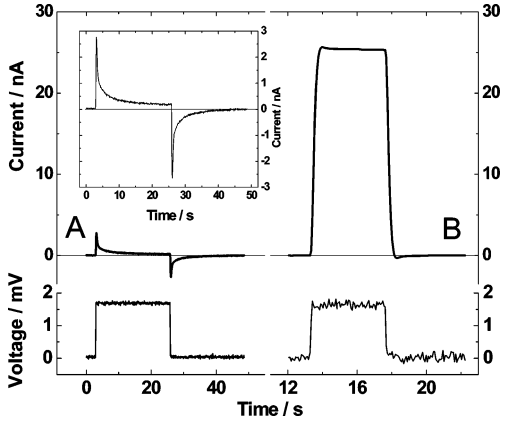

FIGURE 7. Current–time (upper curves) and voltage–time (lower curves) profiles obtained for a S–Ni(OH)$_2$ microparticle (30 μm diameter) in 9 M KOH polarized at 0.22 V (curve A reduced) and subsequently at 0.45 V (oxidized) following application of a pulse drain voltage of ca. 1.7 mV. Inset: Same as A (upper curve) in an expanded scale.

filled with aqueous 1 M KOH together with a Pt wire as counter and a saturated calomel (SCE) as reference electrodes.

Shown in Figure 5 are a series of consecutive voltammetric curves obtained for a single s-Ni(OH)$_2$ μ-particle and

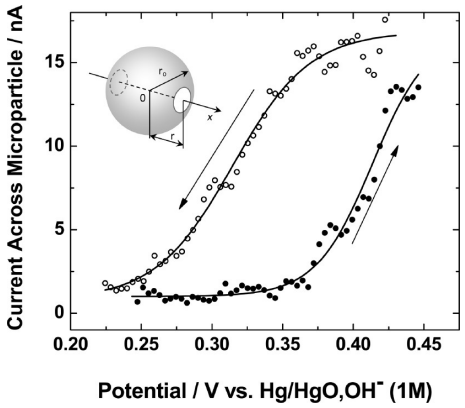

FIGURE 8. Plot of the current through the microparticle as a function of the applied potential while the microparticle was cycled between the specified limits. The continuous lines are best fits to the experimental data points. Inset: Sphere of radius r_0, with opposite flattened ends at $x = r$.

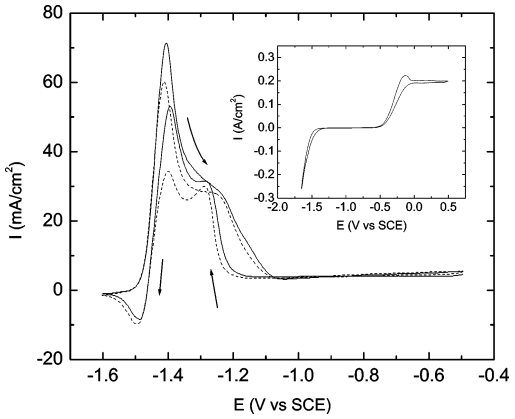

FIGURE 9. First (solid line) and second (dash line) cyclic voltammograms ($v = 50$ mV/s) of a Zn microparticle attached to a polymer-coated W tip in nondeareated 1 M KOH. Inset: Cyclic voltammogram of a bare (uncoated) W tip recorded under otherwise identical conditions.

that of the featureless bare substrate (see red curve). As evident from these data, a potential $E > 0.55$ V vs SCE was required during the first scan in the positive direction for any measurable current to flow, a behavior attributed to the highly resistive character of pristine Ni(OH)$_2$. In contrast, clear peaks associated with the formal Ni(OH)$_2$|NiOOH redox transition centered at 0.38 (oxidation) and 0.21 V (reduction) vs SCE could be observed during the second and subsequent cycles.

In addition, Ni hydroxide exhibits electrochromic properties; that is, its color changes from transparent (reduced state) to deep blue (oxidized state). Shown in the lower panels in Figure 4 are images collected at the specified potentials during a video session for a pristine s-Ni(OH)$_2$ particle while it was being scanned from 0.0 to ca. 0.53 V vs SCE and back. As indicated, continuous oxidation of the μ-particle was accompanied by the gradual emergence of a dark section next to the μ-electrode which advanced toward

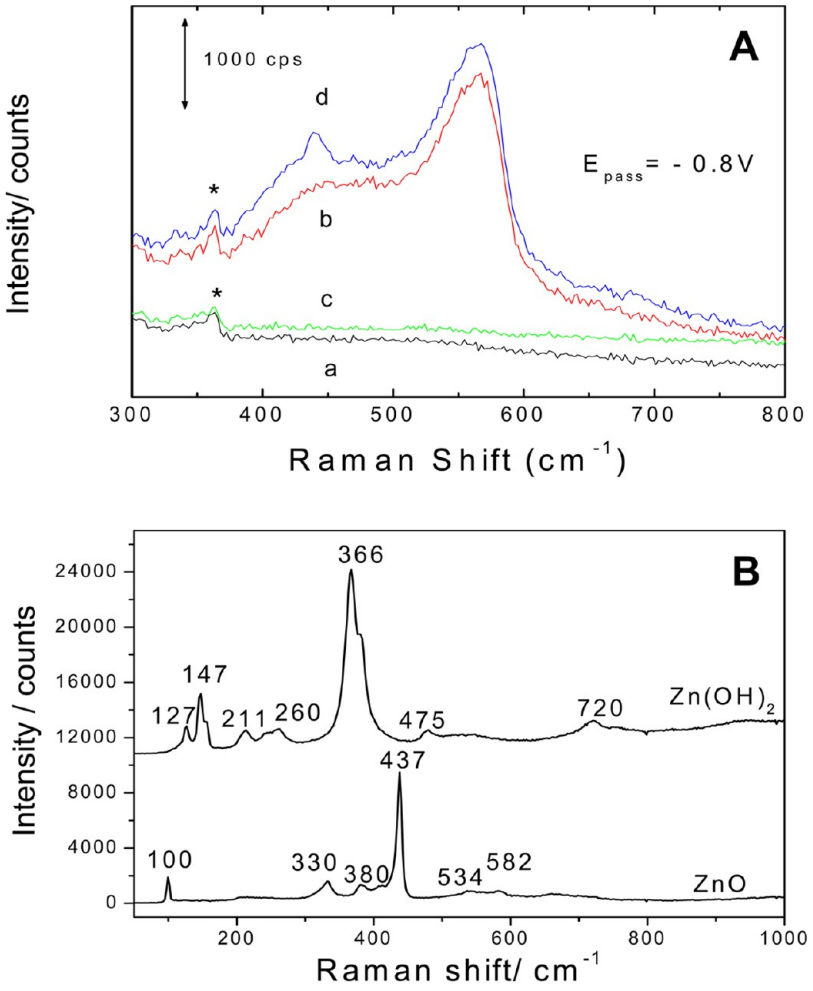

FIGURE 10. Panel A: Set of water-band normalized in situ Raman for a fresh (not cycled) Zn particle ca. 120 μm in diameter (ϕ) polarized at $E_0 = -1.55$ V (curve a), following passivation at $E_{pas} = -0.8$ V after passing a total charge $Q_{pas} = 2.88$ mC/cm^2 (curve b), after subsequent polarization at E_0 for 15−20 min (curve c), and following repassivation at $E_{pas}^{'} = -0.8$ V after passing the same Q_{pas}. Panel B: Ex situ Raman spectra for ZnO and $Zn(OH)_2$ powders.

the holding tool until the whole particle acquired a homogeneously dark appearance.

Measurements of the resistance of a single microparticle of s-$Ni(OH)_2$ were performed in situ as a function of the state of charge using an arrangement similar to that shown in the upper panel Figure 4, in which the holding tool was replaced by a second Au μ-disk electrode trapping the microparticle in between (see Figure 6).[8] Shown in Figure 7 are current versus time (upper curves) obtained for a s-$Ni(OH)_2$ μ-particle in a 9 M KOH, following application of a voltage pulse of ca. 1.7 mV across (lower curves) the μ-particle, while the latter was being polarized at 0.22 V (reduced state) and 0.45 V (oxidized state) vs $Hg/HgO,OH^-$. Much smaller currents were observed for the reduced compared to the oxidized states, indicating that the resistance of the former is higher than that of the latter, as has been reported from data collected ex situ by other techniques. The conductivity, σ, of a flat ended solid sphere (see insert Figure 8) of radius r_0 and resistance R can be expressed as

$$\sigma = \frac{1}{\pi r_0 R} \ln\left(\frac{r_0 + r}{r_0 - r}\right) \quad (1)$$

where r is the distance between the center of the sphere and the center of the flat disks, $r < r_0$. Based on the results displayed in Figure 7, R(reduced) = 10 MΩ and R(oxidized) = 60 kΩ; hence, assuming, $r_0 = 15$ μm and $r = 1$ μm, eq 1 would predict values of σ of 7×10^{-5} and 1.2×10^{-2} S·cm^{-1}, respectively, which are well within values reported elsewhere.[9]

b. Metallic Zinc. Zinc electrodes in $Zn|MnO_2$ batteries consist of particles tens of micrometers in characteristic dimensions dispersed in a concentrated aqueous KOH solution mixed with a polymer.[10] In situ Raman spectra were recorded by inserting an electrochemically sharpened

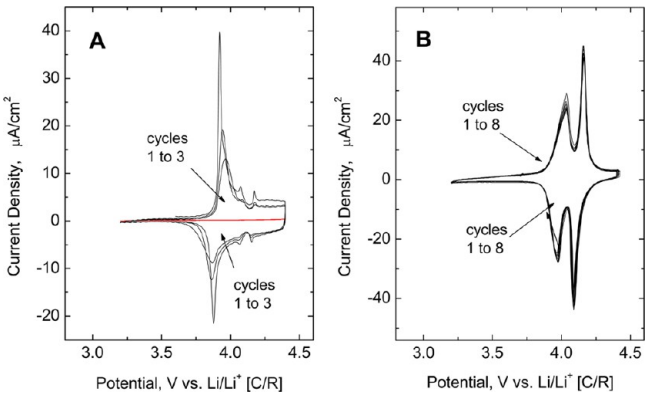

FIGURE 11. Sequence of cyclic voltammetric scans for the $LiCoO_2$ (panel A) $LiMn_2O_4$ (panel B) recorded in 1 M $LiPF_6$ in 2:1 EC|DMC at a scan rate $\nu = 0.04$ mV/s. The thin solid line in panel A represents the cyclic voltammetric response of the Au foil current collector after dissolving the $LiCoO_2$ particles in HCl and further drying.

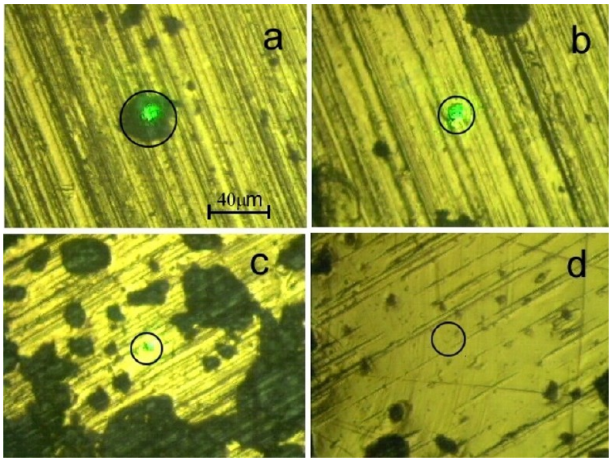

FIGURE 12. Optical images obtained with the Raman microscope of areas of a Au foil electrode with embedded $LiMn_2O_4$ particles with the electrode polarized at 4.4 V vs Li[C/R]. The lighter spot in the center of the circle (not clearly seen in panel d) represents the area of the electrode being illuminated by the laser beam. Panels a–c show the laser beam impinging on particles of a $\phi = 30\ \mu$m (a), 8 μm (b), and 4 μm (c). The circle in panel d represents an area of the electrode devoid of particles.

tungsten tip coated with a thin and polymer layer exposing only its tip (see panel B, Figure 1) into a single Zn particle harvested from a Zn/MnO_2 battery. Tungsten displays a featureless voltammogram in 1 M KOH (see inset, Figure 9) within the potential range in which Zn undergoes active dissolution (see Figure 9) and, as such, is an ideal substrate for studies of this type. In situ Raman measurements were performed in a shallow Petri dish under the microscope.[11] Prior to the spectroelectrochemical experiments, the fresh Zn microparticle was polarized at a potential $E_0 = -1.55$ V vs SCE to reduce the native surface oxide. Shown in Figure 10

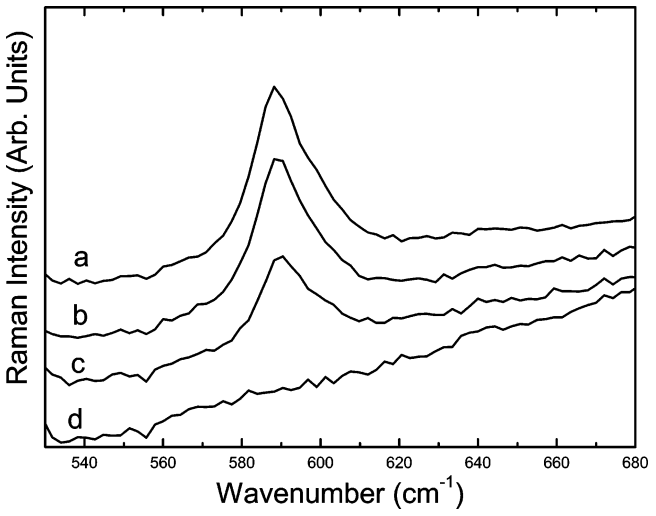

FIGURE 13. Raman spectra of embedded particles shown in panels a–d in Figure 12, while holding electrode potential at 4.4 V vs Li[C/R], i.e. fully charged state.

are in situ Raman spectra collected for a fresh Zn microparticle in 1 M KOH at E_0 (curve a) and after stepping to $E_{pas} = -0.8$ V (curve b, passive region), allowing a charge of 2 mC/cm^2 to flow. The spectrum at -0.8 V displayed a broad shoulder and a peak in the region between 350 and 610 cm^{-1}, and thus quite different from that of crystalline ZnO or $Zn(OH)_2$ acquired ex situ (see panel B, Figure 10). The unusually high intensity of the peak at ca. 565 cm^{-1}, ascribed to a special kind of collective vibrational mode of excitation of atoms or molecules in condensed matter, that is, E1 longitudinal optical phonon in this case, is consistent with the presence of interstitial Zn and oxygen deficiencies in ZnO.[12]

The electrode was then polarized at E_0 to reduce the oxide and subsequently repassivated using the same protocol above and in situ Raman spectra recorded at each step (see curves c and d in Figure 10, respectively). As shown, the spectrum of the repassivated electrode was very similar to that found following the first passivation, except for a new rather sharp peak at 440 cm^{-1} characteristic of crystalline ZnO.

2. Nonaqueous Systems. Our initial studies in the nonaqueous electrolyte area focused on the development of techniques for the electrochemical and Raman characterization of microparticles of lithiated transition metals oxides and carbonaceous materials, used, respectively, as cathodes and anodes in commercial Li-ion batteries, in the absence of binders or conductivity enhancers. The strategy we employed involved embedding a small number of μ-particles into Au for the cathodes and thermally softened Ni, for the anodes, using high pressure. Ni is particularly suited for the

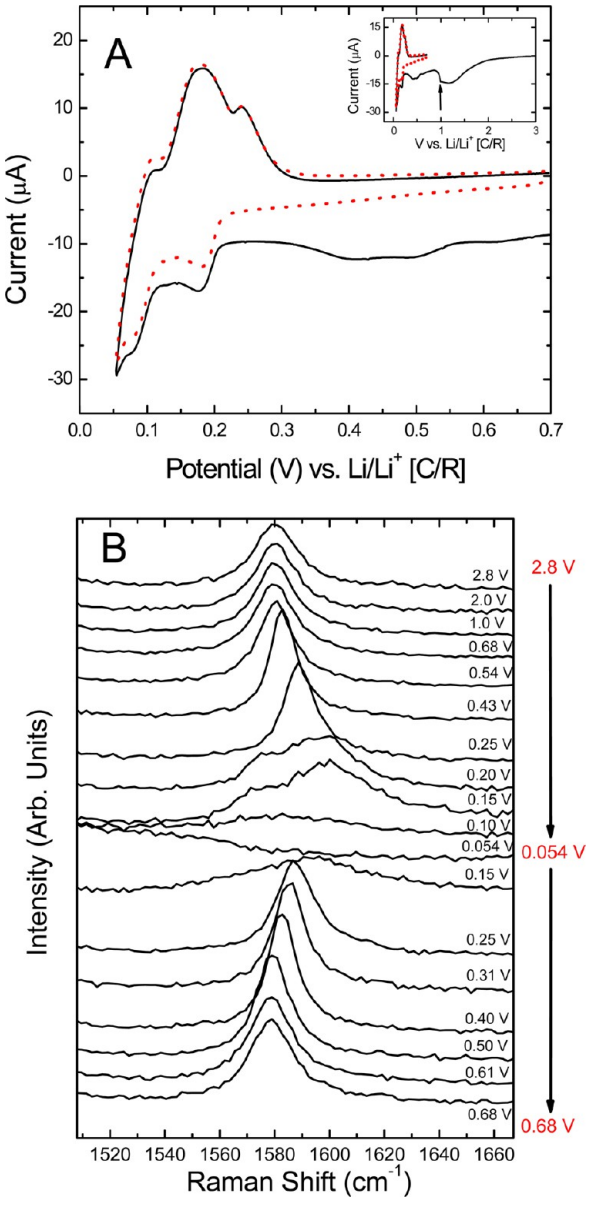

FIGURE 14. Panel A: First (solid line) and second (dotted line) cyclic voltammogram of KS-44 graphite particles embedded into a thermally annealed Ni foil in 1 M $LiClO_4$ in EC/DEC (1:1 v/v) solutions. The first scan was initiated at the measured open circuit potential of the pristine material, i.e., 2.8 V, at $\nu = 0.3$ mV/s. As the potential reached ca. 1 V vs Li/Li^+, the rate was decreased to 0.1 mV/s for the rest of the experiments. Panel B: Series of in situ Raman spectra acquired during the first linear scan in the negative (2.8 down to 0.054 V) and subsequent positive directions (up to 0.68 V) (panel A) with the microscope focused onto a single KS-44 particle ϕ ca. 14 μm recorded while scanning the potential.

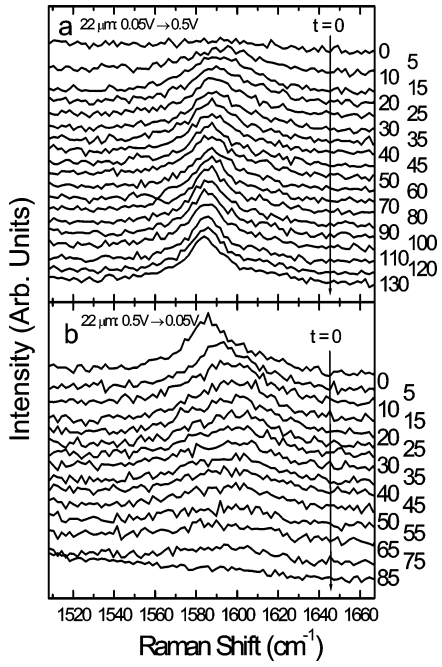

FIGURE 15. In situ, time-resolved Raman spectra collected every 5 s immediately following application of a potential step (PS) for a single 22 μm KS-44 particle, PS 0.05 V → 0.5 V (panel a) and PS 0.5 V → 0.05 V, respectively (panel b).

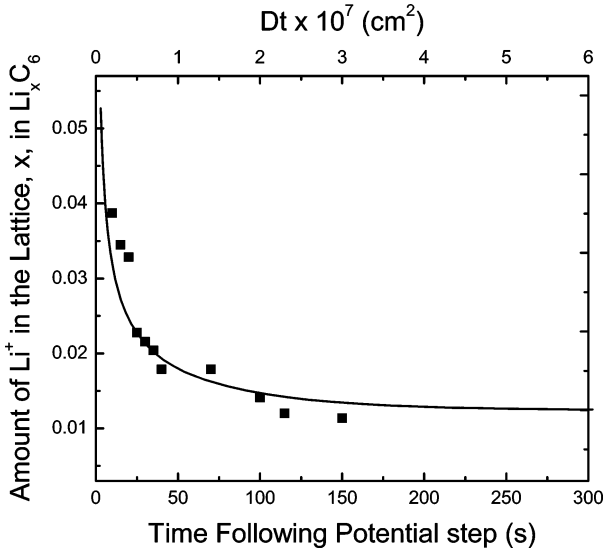

FIGURE 16. Amount of Li^+ in the graphite lattice in dilute stage 1 phase as a function of time after application of a potential step for a single particle ϕ ca. 22 μm, and best fit based on a diffusional model assuming the particle to be a perfect sphere.

study of anodes as it does not form alloys with Li at room temperature. Shown in Figure 11 are a series of sequential voltammetric curves for embedded particles of $LiCoO_2$ |Au (panel A) and $LiMn_2O_4$|Ni (panel B), recorded in 1 M $LiPF_6$ in 2:1 ethylene carbonate (EC)|dimethyl carbonate (DMC), a common base electrolyte used in commercial Li^+ batteries.[13]

The two oxide materials displayed characteristic features associated with the release (charge) and intercalation (discharge) of Li^+ from and into the oxide lattice during the scans in the positive and negative direction, respectively.[14,15] Cycling of the material in the case of $LiCoO_2$ (panel A) gave

rise to changes in the amplitudes of the peaks resulting from modifications in the lattice structure induced by Li^+ insertion and deintercalation. In contrast, hardly any changes were observed in the case of $LiMn_2O_4$ (panel B) upon cycling. Plots of the peak current vs $\nu^{1/2}$ were found to be linear with slopes consistent with an effective "average" diffusion coefficient for Li^+ in the oxide lattice of ca. 5×10^{-10} cm^2/s which is in line with those measured by other means.[16]

Shown in Figure 12 are optical images of areas of a Au electrode with embedded $LiMn_2O_4$ particles (dark regions),[17] where the bright spot, ϕ_{fp} ca. 5 μm, is the laser footprint on the sample. The ability of Raman microscopy to focus the light over a very small area enables situ Raman spectra of individual particles to be recorded as a function of the applied potential. Shown in Figure 13 is the Raman spectrum obtained for a single embedded $LiMn_2O_4$ particle, ϕ, ca. 30 μm, in the same electrolyte specified above using a cell similar to that in Figure 2. Spectra collected at 4.4 V vs $Li^+|Li$, that is, fully charged state, yielding a well-defined Raman peak centered 590 cm^{-1} characteristic of this material (vide infra).

The same overall technique was utilized for in situ Raman studies of carbonaceous micromaterials embedded in softened Ni in 1 M $LiClO_4$ in 2:1 EC|DEC solutions.[18,19] Excellent agreement with literature data collected by other means[14] was obtained for in situ Raman spectra as a function of the applied potential for a single particle of KS-44 (ϕ ca. 14 μm), a commercially available graphitic powder, while scanning the potential at $\nu = 0.3$ mV/s first in the negative direction from 2.8 down to 0.054 V, and, subsequently, in the positive direction up to 0.68 V (see panel A, Figure 14). The spectroscopic data are displayed in panel B in the same figure, where the potential next to each of the spectra represents average values during spectral acquisition. As has been documented,[20] insertion of Li^+ in the lattice brings about changes in the spectral features observed. In particular, a direct correlation was found between the position of the G band in the range $1581-1590$ cm^{-1}, and the amount of Li^+ within the so-called dilute stage 1 phase, using as a basis the X-ray diffraction (XRD) data reported by Dahn,[21] who monitored current and voltage during galvanostatic charging in similar electrolytes. This correspondence was used to determine the rates of insertion and release of Li^+ from the graphite lattice as a function of the applied potential.[18] For these experiments, a potential step was applied between 0.05 V (nominally full Li^+ intercalation and 0.5 V (full Li^+ deintercalation) while recording in situ Raman spectra yielding data of the type shown in Figure 15. Statistical analysis of

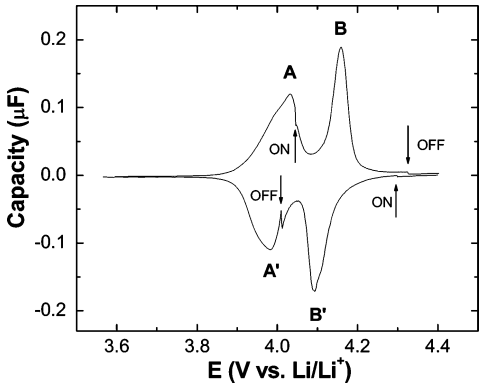

FIGURE 17. Capacity vs *E* data extracted from the third cyclic voltammogram (CV) of a single $LiMn_2O_4$ microparticle recorded at ν ca. 0.11 mV/s (see text for details) in a 1 M $LiClO_4$ solution in a mixture of ethylene carbonate (EC) and diethyl carbonate (DEC) (1:1 by volume) in the spectroelectrochemical cell *during* acquisition of Raman spectra. The focused laser beam was turned ON and OFF as indicated.

these spectra enabled determination of the average transient concentration of Li^+ in a volume within a very thin shell of the particle probed by the laser. The latter were then fit to a diffusional model assuming the particle to be a perfect sphere yielding an effective diffusion coefficient of ca. 2×10^{-9} cm^2/s (see Figure 16), and thus similar tothat measured by other means.[16]

a. Single Particle MicroRaman Spectroelectrochemistry. Methods of the type described in previous sections were implemented to attach a single microparticle to the surface of a microelectrode and thus allow correlations between the current and the spectral features associated with that single microparticle.The following subsections summarize the results we obtained for a single graphite microflake and for particles of $LiMn_2O_4$ both in polycrystalline (poly) and single crystal forms.

Lithium Mn Oxide. Shown in Figure 17 are capacitance versus *E* data derived from the voltammogram of a single $LiMn_2O_4$(poly) microparticle recorded in a 1 M $LiClO_4$ solution in a mixture of EC|DEC (1:1 by volume) in the spectroelectrochemical cell in Figure 1 *during* acquisition of in situ Raman spectra (see Figure 18).[6] The focused laser beam was turned ON and OFF at the potentials specified by the arrows in the curve. The labels next to each of the spectra are the average potentials during the spectral acquisition, whereas SOD represent the state of discharge of the particle in percent, that is, 0, for $E = 4.30$ V (fully charged) and 100, for $E = 3.60$ V (fully discharged). Based on the use of chemometric techniques, the broad, and markedly asymmetric feature centered at ca. 600 cm^{-1} found for $4.021 < E < 4.118$ V (panels C and D, Figure 18) can be ascribed to two T_2 and two A_1 modes of $Li_{0.5}Mn_2O_4$,[22,23] whereas the two

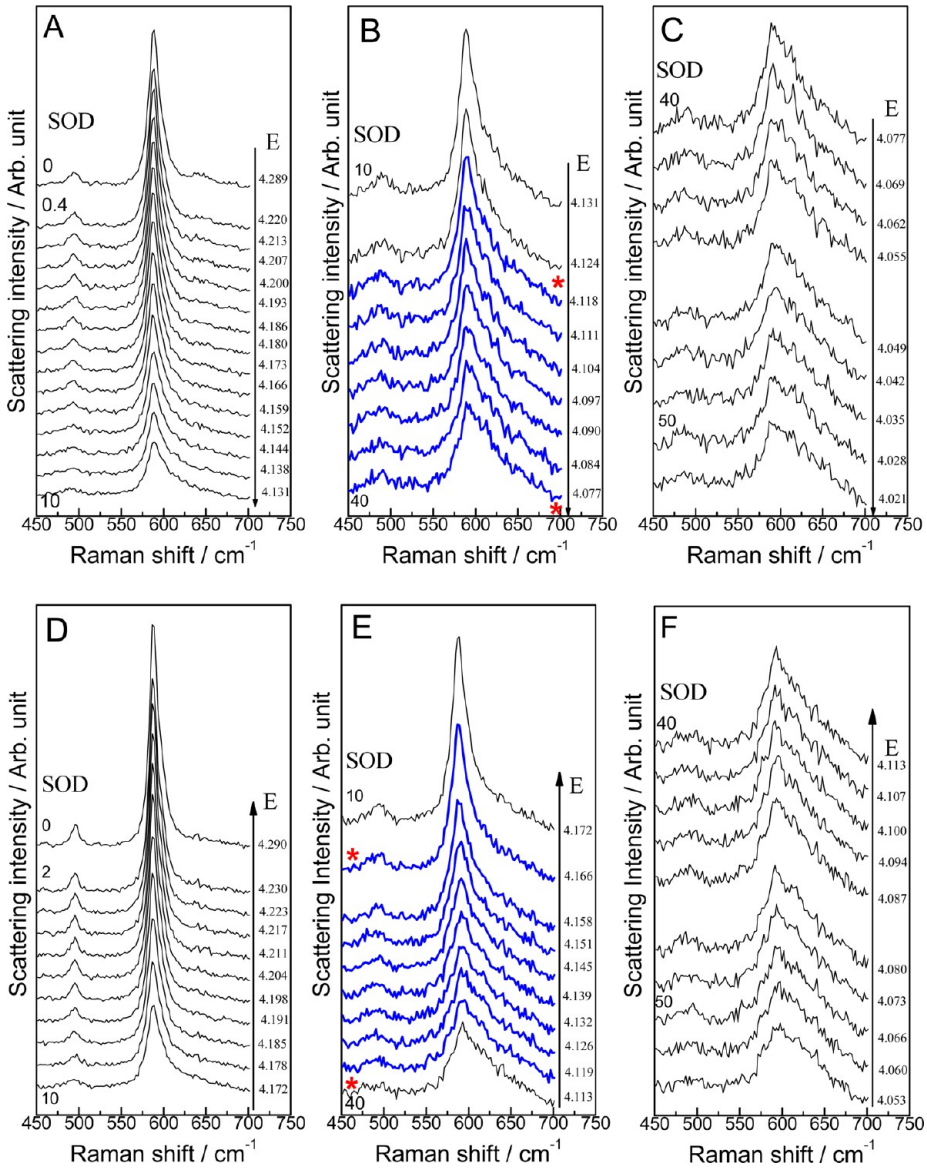

FIGURE 18. Series of Raman spectra recorded while acquiring the cyclic voltammetry data for the single $LiMn_2O_4$ microparticle in Figure 17 for the scan in the negative (panels A–C) and positive (panels D–F) directions. The average potential, *E*, during each spectral collection is indicated on the right, whereas selected values of the state of discharge (SOD, %) are shown on the left side of the curves. The spectra in thicker blue lines were used for quantitative analyses of phase composition (see Figure 19).

prominent peaks centered at 495 and 588 cm^{-1}, attributed to the $T_{2g}(2)$ and A_{1g} modes of λ-MnO_2, respectively, could be discerned in the spectra for $E > 4.131$ V (see panels A and B, Figure 18). The increase in scattering intensity in the region of 450–700 cm^{-1} for $E > 4.172$ V (up to 4.29 V, see panel C) has been attributed to resonance enhancement effects associated with λ-MnO_2.[22]

In situ XRD measurements reported by Eriksson et al. for $Li_xMn_2O_4$,[24] afforded strong evidence for the presence of a single phase over the range $0 < SOD < 11\%$ (phase 1), and a different single phase, 2, over $35 < SOD < 100\%$, and for the coexistence these two phases in the intermediate range $11 < SOD < 35\%$, for which their respective lattice parameters remained fixed at 8.805 and 8.145 Å. As shown in Figure 18, large drops in intensity were found in the Raman spectra recorded during the initial stages of discharge of the fully charged microparticle in which the only phase present (phase 1) undergoes a linear lattice expansion as a function of the SOD.

More amenable to a rigorous analysis, however, are spectral data acquired in the intermediate SOD range, where the lattice parameters of the two phases are independent of the SOD. To this end, the Raman spectra collected at SOD = ca. 16% and ca. 43% were assumed to represent the pure phases 1 and 2, respectively, and *no restrictions were imposed*

while fitting the data on the sum of the constituent phases for each SOD. Spectra used for analysis are indicated by thicker lines and pure phases by a star in panels B and E in Figure 18. In analogy with the conclusions made by Eriksson et al.[24] based on their in situ XRD studies, the results derived from the statistical treatment of the Raman data for the microparticle yielded good linear correlations ($R > 0.99$) between the fraction of each constituent phase and the SOD (see Figure 19). Furthermore, the *unrestricted* sum of the components correctly predicts (within 2%) values very close to 1, lending strong support to the validity of the method implemented. Similar results were also obtained using single crystal $LiMn_2O_4$.[25]

Graphite Flake. Shown in panels A through E in Figure 20 are a series of in situ Raman spectra recorded continuously for a KS-44 graphite microflake ϕ ca. 50 μm and ca. 1 μm thick 1 M $LiClO_4$ solution in a DEC/EC mixture (1:1 by volume) during the fourth linear voltammetric scan in the negative direction (see Figure 21).[26] Both the Raman and electrochemical data were found to be in excellent agreement with results reported by other groups using more conventional electrodes.[20,27] In particular,

(i) The Raman spectra of the KS-44 microflake down to ca. 0.22 V (see panels A–C), exhibit a single prominent peak at 1580 cm^{-1} ascribed (primarily) to the E_{2g2} mode of graphite.

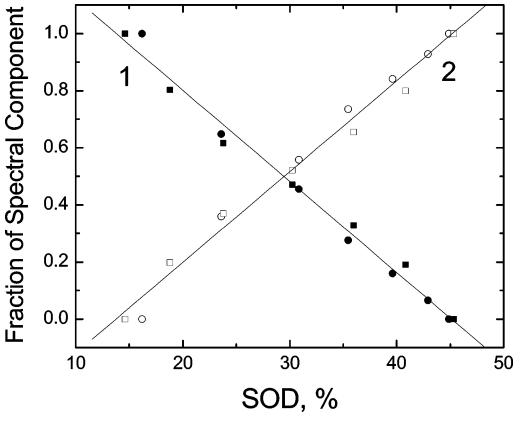

FIGURE 19. Plots of the fraction of the spectral component of phase 1 (solid symbols) and phase 2 (open symbols) for data collected during the scan in the negative (circles) and positive (squares) scans based on a statistical analysis of the spectra shown in blue thick lines in Figure 18.

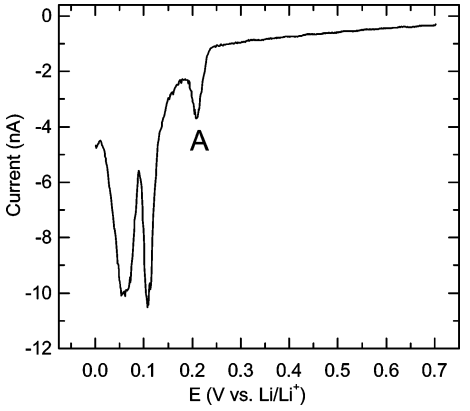

FIGURE 21. Fourth linear voltammetric scan recorded in the negative direction at a scan rate of 0.1 mV/s while acquiring the in situ Raman data in Figure 20.

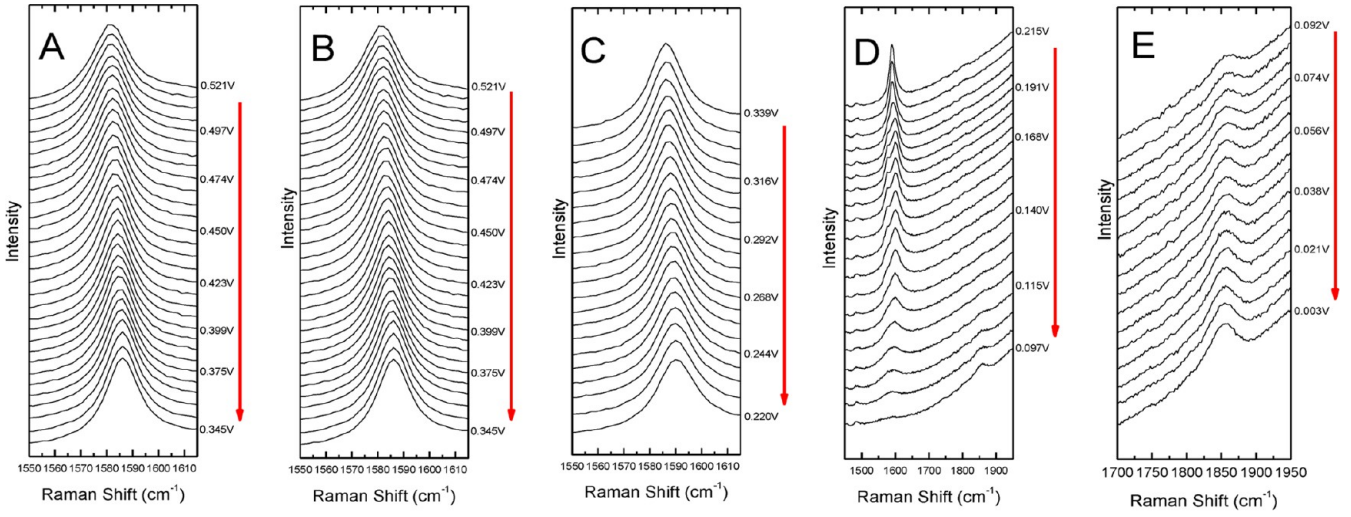

FIGURE 20. Series of in situ Raman spectra for a KS-44 graphite microflake recorded in 1 M $LiClO_4$ solution in a DEC/EC mixture (1:1 by volume) while acquiring the fourth linear voltammetric scan in the negative direction at a scan rate of 0.1 mV/s shown in Figure 21. The difference in average potential between two adjacent spectra is 6 mV. The arrows on the right-hand side of each panel indicate the direction of the scan.

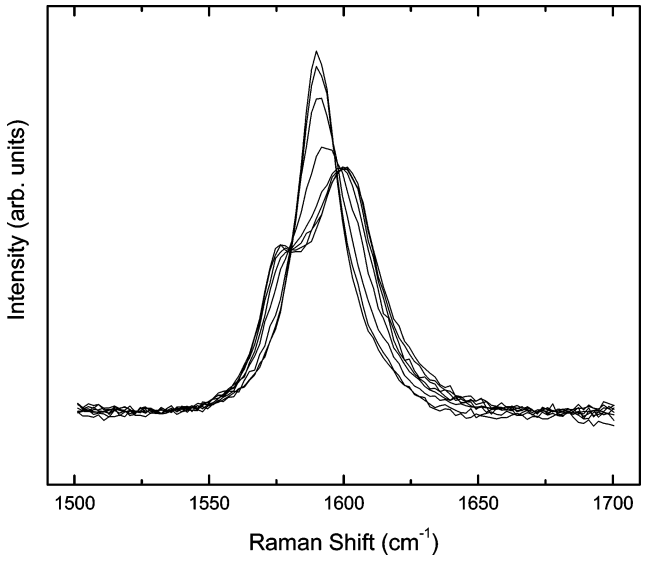

FIGURE 22. In situ Raman spectra in the potential region in which dilute stage 1 and stage 4 coexist, i.e., 0.215−0.174 V vs Li/Li^+ displayed in overlapping form to illustrate the presence of two clear isosbestic points at ca. 1580 and 1598 cm^{-1}.

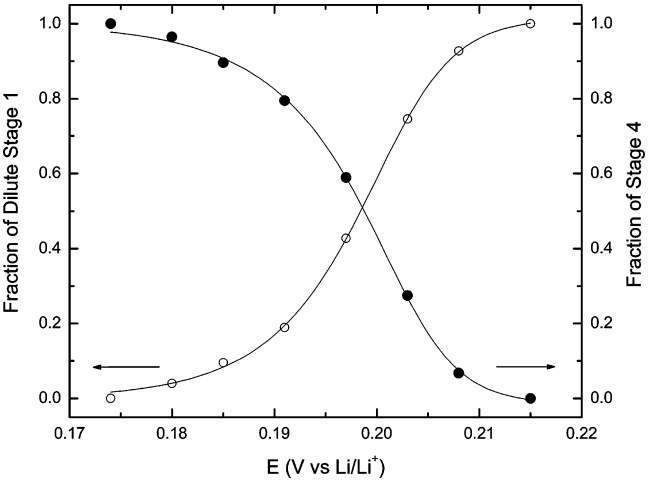

FIGURE 23. Plots of amount of the fraction of dilute stage 1 (left ordinate) and stage 4 (right ordinate) determined *independently* based on the statistical analysis of spectral data as shown in Figure 22. Stage 1 and stage 4 phases are given by the spectra recorded at $E = 0.215$ and 0.157, respectively. The solid lines are best fits the data using arbitrary nonlinear functions.

(ii) At potentials between 0.25 and 0.20 V, the E_{2g2} feature (see panel D, Figure 20) was found to gradually disappear, leading to the simultaneous emergence of two peaks centered at around 1601 and 1577 cm^{-1} (see below) attributed, respectively, to bounding and interior modes of stage 4 of the Li-graphite system.[27]

Strong evidence for a *quantitative* interconversion between stage 1 and stage 4 was obtained from the presence

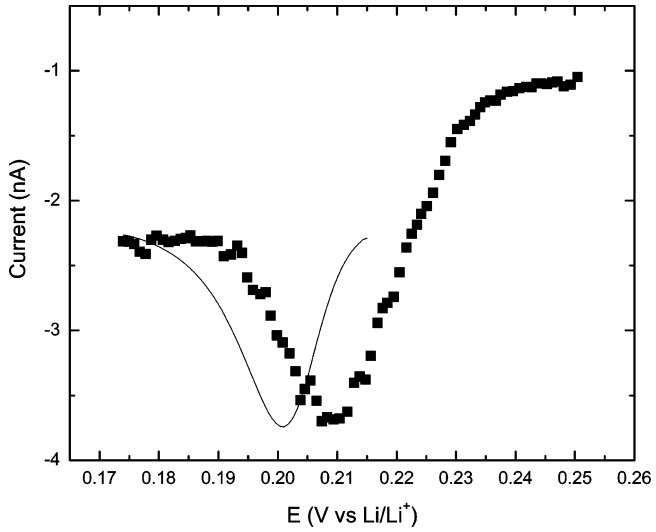

FIGURE 24. Expanded plot of the voltammetric data in Figure 21 in the range ca. $0.175 < E < 0.25$ V (scattered points) and normalized voltammetric peak as deduced from the statistical analyses of the spectroscopic data in Figure 22 (solid line). See text for details.

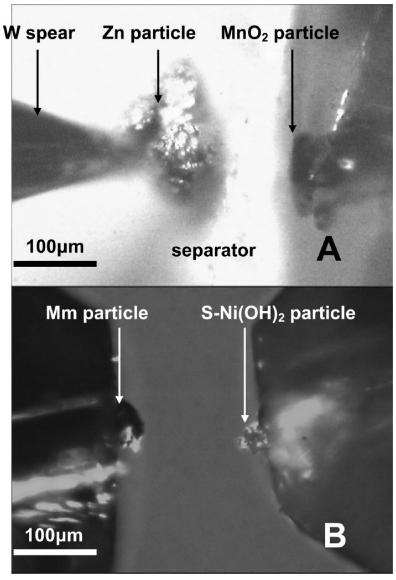

FIGURE 25. Micrographs of assembled Zn|MnO_2 (panel A) and Ni|MH (panel B) microbatteries. The separator in panel B was not included for clarity.

of two clearly defined isosbestic points at 1597 and 1580 cm^{-1} for spectra collected in the range $0.215 \leq E \leq 0.157$ V, (see Figure 22). Stage 1 in this context refers to Li^+ occupying randomly available sites between graphene layers, whereas stage 4 is a phase which contains four graphene planes per unit cell or, equivalently, Li^+ is present only between every fourth pair of graphene planes. It becomes then possible to extract by statistical means the amounts of each of the phases as a function of the applied potential, assuming the

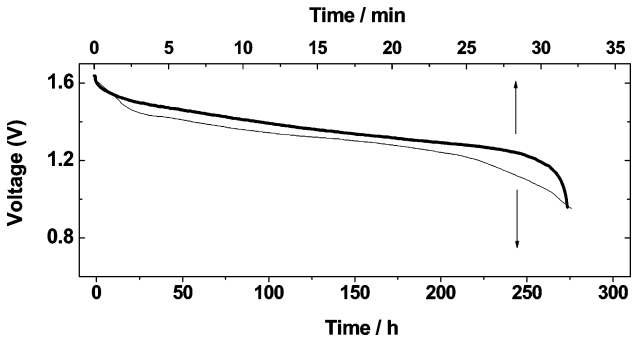

FIGURE 26. Discharge curve for a Zn|MnO_2 microbattery incorporating single particles of Zn (ca. 150 μm diameter) and MnO_2 (ca. 30 μm mean diameter) (see thick line and text for details) in 9 M KOH recorded upon application of a constant current of 48 nA (ca. 2 C). Shown in thin line in the same figure is a discharge curve for a commercial AA Energizer battery at a rate of ca. C/330.

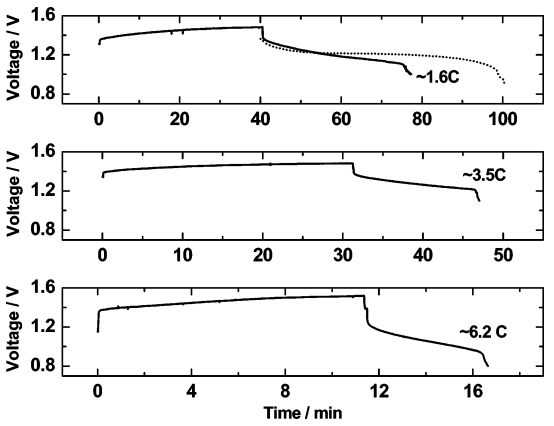

FIGURE 27. Charge–discharge curves for a Ni|MH microbattery (S–Ni$(OH)_2$ ca. 30 μm in diameter; Mm ca. 75 μm mean diameter) at three different *C* rates: 1.6 (A), 3.5 (B) ,and 6.2 (C). The dotted lines in panel A are discharge curves for a commercial AAA Energizer battery at a rate of 1 C.

curves at $E = 0.215$ and 0.157 V represent the spectra of pure stage 1 and pure stage 4, respectively.

Plots of the fractions of dilute stage 1 (left ordinate) and stage 4 (right ordinate) determined independently based on the statistical analysis of spectral data shown in Figure 20 are given in Figure 23. As has been pointed out in the literature, the stage 1 → stage 4 transition corresponds to peak A in the linear scan given in Figure 21.

A direct correlation between spectral and electrochemical data can be drawn by first fitting the experimental points in Figure 23 to an arbitrary nonlinear function and then taking the derivative. The results of such an analysis yielded two virtually identical peaks of different polarity derived either from stage 1 or *independently* from stage 4. The full width at half height (fwhh) of either one of these derivatives renormalized so as to match the current maximum in peak A in

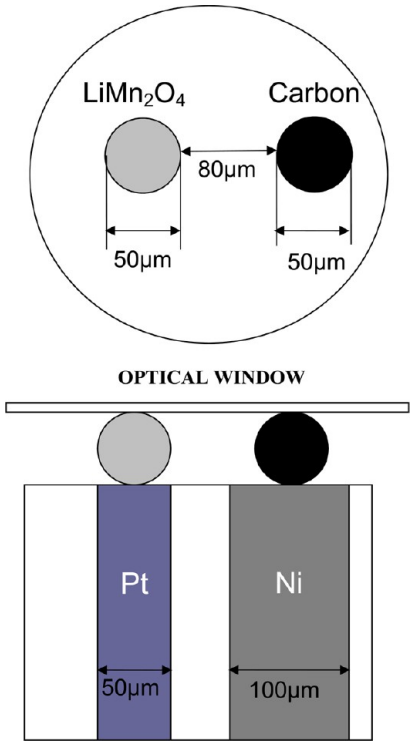

FIGURE 28. Schematic diagram of the dual Pt/Ni microelectrode arrangement involved in the assembly and electrochemical characterization of single microparticle Li^+ batteries.

the voltammogram (see solid curve in Figure 24), were found to be in excellent agreement to that of the voltammetric peak (see scattered points in Figure 24). The peak position extracted from the spectral data, however, is about 10 mV more negative than that in the actual voltammogram. This phenomenon is caused by a diffusional delay; that is, the scan rate is too fast compared to the time constant for mass transport of Li^+ within the graphite lattice.

More recently, Dokko et al.[28] reported closely related experiments using single particles of mesocarbon microbeads (MCMB) and found very high rate capabilities and good charge storage reversibility.

Single Particle Electrode Microbatteries. The same strategies developed for the manipulation of charge storage μ-particles were used to assemble single particle μ-batteries.[5,29] Shown in Figure 25 are photographs of a Zn|MnO_2 (panel A) and Ni$(OH)_2$|MH (panel B), where the separator was omitted for clarity. Electrochemical tests were carried out by immersing the entire assembly into a 9 M KOH solution. A performance assessment of commercial batteries usually involves applying a constant current to the battery while monitoring the potential across it. The rates of discharge are given in terms of C units, where 1 C corresponds to a full discharge in one hour.

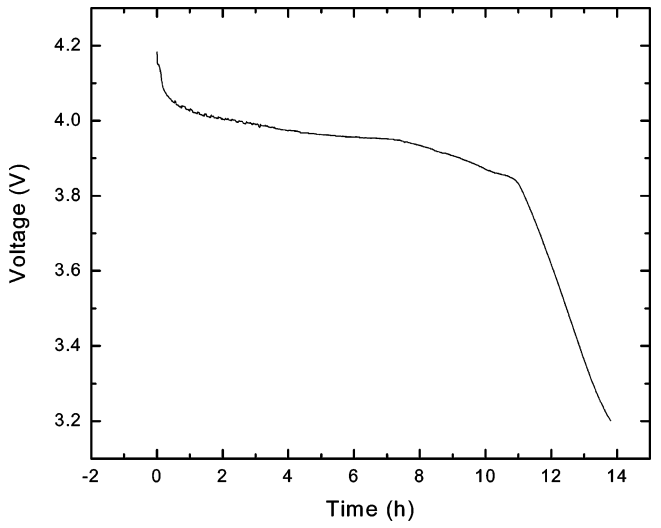

FIGURE 29. Self-discharge of a MCMB/$LiMn_2O_4$ microbattery following individual charging of the two microparticle electrodes.

Aqueous. Shown in Figure 26 (thick line) is a voltage versus time discharge curve for a Zn|MnO_2 μ-battery incorporating single particles of Zn ca. 150 μm diameter, and MnO_2, ca. 30 μm mean diameter, in 9 M KOH recorded upon application of a constant current of 48 nA, which based on the limiting electrode, would correspond to a discharge rate of ca. 2 C. Corresponding curves for a $Ni(OH)_2$|MH incorporating a spherical $Ni(OH)_2$ particle ca. 30 μm in diameter and a MH particle ca. 75 μm in diameter, recorded at three *C* rates, 1.6 (A), 3.5 (B), and 6.2 (C), are shown in Figure 27. The dotted lines in panel A represent discharge curves obtained from commercial batteries and support the view that data collected from these single particle μ-batteries closely mimic those found for technical devices.

Nonaqueous. Single μ-particle $LiMn_2O_4$/carbon batteries were assembled by placing individual cathode and anode particles onto two isolated microelectrodes encased in a single glass rod (see Figure 28), which was inserted into the cell in Figure 2 filled with 1 M $LiPF_6$ in EC/DEC (1:1) electrolytes. The self-discharge of the battery was monitored by measuring its potential as a function of time after the two microparticles in the battery had been fully charged independently. As shown in Figure 29, the potential was very stable for about 10 h, that is, 3.9 V average, dropping significantly thereafter, a phenomenon associated in all likelihood with the carbon electrode.

Concluding Remarks and Future Prospects

Much of the initial impetus of the work highlighted in this Account was aimed at developing means of correlating the state of charge of battery microparticles with their spectroscopic characteristics, as a first step toward monitoring the flow of charge within electrodes in actual operating batteries in real time. An intriguing approach being pursed in our laboratories involves the use of Raman microscopy to raster the edge surface of an operating battery during charge and discharge. Despite our initial success,[30] further refinements will be required before the results of such experiments could be compared with theoretical models proposed in the literature to simulate the macroscopic behavior of actual devices.

This work was supported by DOE, NASA and Eveready Battery Company.

BIOGRAPHICAL INFORMATION

Adriel J. J. Jebaraj received his B.S. in chemical and electrochemical engineering from the Central Electrochemical Research Institute, Karaikudi, India in 2009. He is now a Ph.D. student in the Department of Chemistry at Case Western Reserve University. His current research interests focus on electrocatalysis and in situ spectroscopic techniques

Daniel Scherson received his License in Chemistry from the University of Chile and his Ph.D. in chemistry from University of California, Davis. He is the Frank Hovorka Professor of Chemistry at Case Western Reserve University and Director of the Ernest B. Yeager Center for Electrochemical Sciences. His current interests are in the areas of in situ spectroscopy and fundamental aspects of electrocatalysis, and energy conversion and storage.

FOOTNOTES

*To whom correspondence should be addressed.
The authors declare no competing financial interest.

REFERENCES

1 Winter, M.; Brodd, R. J. What are batteries, fuel cells, and supercapacitors? *Chem. Rev.* **2004**, *104*, 4245–4269.
2 Dokko, K.; Mohamedi, M.; Umeda, M.; Uchida, I. Kinetic study of Li-ion extraction and insertion at $LiMn_2O_4$ single particle electrodes using potential step and impedance methods. *J. Electrochem. Soc.* **2003**, *150*, A425–A429.
3 Kim, H. S.; Itoh, T.; Nishizawa, M.; Mohamedi, M.; Umeda, M.; Uchida, I. Microvoltammetric study of electrochemical properties of a single spherical nickel hydroxide particle. *Int. J. Hydrogen Energy* **2002**, *27*, 295–300.
4 Baddour-Hadjean, R.; Pereira-Ramos, J.-P. Raman Microspectrometry Applied to the Study of Electrode Materials for Lithium Batteries. *Chem. Rev.* **2010**, *110*, 1278–1319.
5 Palencsar, A.; Scherson, D. A. Single-particle electrode aqueous microbatteries. *Electrochem. Solid-State Lett.* **2005**, *8*, A622–A626.
6 Dokko, K.; Shi, Q. F.; Stefan, I. C.; Scherson, D. A. In situ Raman spectroscopy of single microparticle Li^+-intercalation electrodes. *J. Phys. Chem. B* **2003**, *107*, 12549–12554.
7 Palencsar, A.; Scherson, D. A. Electrochemical and in situ optical characterization of single micrometer-size particles of spherical nickel oxide in alkaline aqueous electrolytes. *Electrochem. Solid-State Lett.* **2003**, *6*, E1–E4.
8 Palencsar, A.; Scherson, D. A. In situ resistance measurements of single particle spherical $Ni(OH)_2$ microelectrodes as a function of their state of charge. *Electrochem. Solid-State Lett.* **2005**, *8*, A328–A332.
9 Motori, A.; Sandrolini, F.; Davolio, G. Electrical-properties of nickel-hydroxide for alkaline cell systems. *J. Power Sources* **1994**, *48*, 361–370.
10 Zhang, X. G. *Corrosion and Electrochemistry of Zinc*; Plenum Press: New York, 1996.
11 Shi, Q. F.; Rendek, L. J.; Cai, W. B.; Scherson, D. A. In situ Raman spectroscopy of single particle microelectrodes. *Electrochem. Solid-State Lett.* **2003**, *6*, E35–E39.

12 Tzolov, M.; Tzenov, N.; Dimova-Malinovska, D.; Kalitzova, M.; Pizzuto, C.; Vitali, G.; Zollo, G.; Ivanov, I. Vibrational properties and structure of undoped and Al-doped ZnO films deposited by RF magnetron sputtering. *Thin Solid Films* **2000**, *379*, 28–36.

13 Totir, D. A.; Cahan, B. D.; Scherson, D. A. Electrochemical characterization of lithiated transition metal oxide cathode particles in the absence of carbon, binders and other additives. *Electrochim. Acta* **1999**, *45*, 161–166.

14 Tarascon, J. M.; Guyomard, D. Li metal-free rechargeable batteries based on $Li_{(1+x)}Mn_2O_4$ cathodes ($0 \leqslant x \leqslant 1$) and carbon anodes. *J. Electrochem. Soc.* **1991**, *138*, 2864–2868.

15 Uchida, I.; Sato, H. Preparation of binder-free, thin-film $LiCoO_2$ and its electrochemical responses in a propylene carbonate solution. *J. Electrochem. Soc.* **1995**, *142*, L139–L141.

16 Rougier, A.; Striebel, K. A.; Wen, S. J.; Cairns, E. J. Cyclic voltammetry of pulsed laser deposited $Li_xMn_2O_4$ thin films. *J. Electrochem. Soc.* **1998**, *145*, 2975–2980.

17 Luo, Y.; Cai, W.-B.; Scherson, D. A. In Situ Raman Spectroscopy of Single Particle Electrodes. *Electrochem. Solid-State Lett.* **2001**, *4*, A101–A104.

18 Luo, Y.; Cai, W. B.; Scherson, D. A. In situ, real-time Raman microscopy of embedded single particle graphite electrodes. *J. Electrochem. Soc.* **2002**, *149*, A1100–A1105.

19 Totir, D. A.; Scherson, D. A. Electrochemical and in situ Raman studies of embedded carbon particle electrodes in nonaqueous liquid electrolytes. *Electrochem. Solid-State Lett.* **2000**, *3*, 263–265.

20 Huang, W. W.; Frech, P. In situ Raman studies of graphite surface structures during lithium electrochemical intercalation. *J. Electrochem. Soc.* **1998**, *145*, 765–770.

21 Dahn, J. R. Phase diagram of Li_xC_6. *Phys. Rev. B* **1991**, *44*, 9170–9177.

22 Ammundsen, B.; Burns, G. R.; Islam, M. S.; Kanoh, H.; Roziere, J. Lattice dynamics and vibrational spectra of lithium manganese oxides: A computer simulation and spectroscopic study. *J. Phys. Chem. B* **1999**, *103*, 5175–5180.

23 Kanoh, H.; Tang, W. P.; Ooi, K. In situ Raman spectroscopic study on electroinsertion of Li^+ into a Pt/λ -MnO_2 electrode in aqueous solution. *Electrochem. Solid-State Lett.* **1998**, *1*, 17–19.

24 Eriksson, T.; Andersson, A. M.; Bishop, A. G.; Gejke, C.; Gustafsson, T.; Thomas, J. O. Surface analysis of $LiMn_2O_4$ electrodes in carbonate-based electrolytes. *J. Electrochem. Soc.* **2002**, *149*, A69–A78.

25 Shi, Q.; Takahashi, Y.; Akimoto, J.; Stefan, I. C.; Scherson, D. A. In Situ Raman Scattering Measurements of a $LiMn_2O_4$ Single Crystal Microelectrode. *Electrochem. Solid-State Lett.* **2005**, *8*, A521–A524.

26 Shi, Q. F.; Dokko, K.; Scherson, D. A. In situ Raman microscopy of a single graphite microflake electrode in a Li^+-containing electrolyte. *J. Phys. Chem. B* **2004**, *108*, 4789–4793.

27 Inaba, M.; Yoshida, H.; Ogumi, Z.; Abe, T.; Mizutani, Y.; Asano, M. In Situ Raman Study on Electrochemical Li Intercalation into Graphite. *J. Electrochem. Soc.* **1995**, *142*, 20–26.

28 Dokko, K.; Nakata, N.; Suzuki, Y.; Kanamura, K. High-Rate Lithium Deintercalation from Lithiated Graphite Single-Particle Electrode. *J. Phys. Chem. C* **2010**, *114*, 8646–8650.

29 Shi, Q. F.; Scherson, D. A. Single particle electrode microbatteries. *Electrochem. Solid-State Lett.* **2005**, *8*, A122–A124.

30 Luo, Y.; Cai, W.-B.; Xing, X.-k.; Scherson, D. A. In Situ, Time-Resolved Raman Spectromicrotopography of an Operating Lithium-Ion Battery. *Electrochem. Solid-State Lett.* **2004**, *7*, E1–E5.